The NiSi melting curve to 70 GPa

Oliver T. Lord[a],*, Elizabeth T. H. Wann[a], Simon A. Hunt[a], Andrew M. Walker[b,†], James

Santangeli[a], Michael J. Walter[b], David P. Dobson[a], Ian G. Wood[a], Lidunka Vočadlo[a],

Guillaume Morard[c], Mohamed Mezouar[d]

[a]Department of Earth Sciences, University College London, Gower Street, London, WC1E 6BT, UK

[b]School of Earth Sciences, University of Bristol, Wills Memorial Building, Queen's Road, Bristol, BS8 1RJ, UK

[c]Institut de Minéralogie et de Physique des Milieux Condensés UMR CNRS 7590, Université Pierre et Marie Curie,

    75005 Paris, France.

[d]European Synchrotron Radiation Facility, BP 220, F-3804 Grenoble Cedex, France.

[†]Present address: School of Earth and Environment, University of Leeds, Leeds, LS29JT, UK

*Corresponding Author

Present address: School of Earth Sciences, University of Bristol, Wills Memorial Building, Queen's Road, Bristol, BS8

1RJ, UK

Email: oliver.lord@bristol.ac.uk

Phone: +44 117 9545421

Fax: +44 117 9253385

Total number of words in Main text: 7349

Abstract: 222

Number of tables: 2

Number of figures: 9

References: 43

1   **Abstract**

2   The melting curve of NiSi has been determined to 70 GPa on the basis of laser-heated

3   diamond anvil cell (LH-DAC) experiments in which changes in the gradient of temperature vs. laser

4   power functions were used as the melting criterion. The melting curve was corroborated with *in situ*

5   X-ray diffraction experiments in both the LH-DAC and multi-anvil press in which the appearance

6   of liquid diffuse scattering in the diffraction patterns was used as the melting criterion. At all

7   pressures, the NiSi melting curve is lower than that of FeSi, with the difference in melting

8   temperature reaching a maximum of 900 K at 14 GPa. The location of the B31 + B20 + L triple

9   point has been constrained to 12±2 GPa and 1550±100 K and the B20 + B2 + L triple point to

10   28.5±1.5 GPa and 2165±60 K. On the basis of the *in situ* LH-DAC experiments the Clapeyron slope

11   of the B20 → B2 transition is estimated at -67 MPa K^{-1}. Extrapolation of the B2-NiSi liquidus to

12   core-mantle boundary (CMB) conditions (135 GPa) suggests the melting point of NiSi (3700±400

13   K) will be only marginally lower than that of isostructural FeSi (4000±200 K). Thus any (Fe,Ni)Si

14   solid solution present within the D″ layer is expected to remain solid, with the possible exception of

15   the very hottest region adjacent to the CMB.

16

17   **Keywords:** NiSi, melting, high-pressure, *in situ*, LH-DAC

1. Introduction

Historically, the primary interest in nickel monosilicide (NiSi), an intermediate compound along the Ni-Si binary (Massalski et al, 1990), owed to its usefulness as a contact material in microelectronic devices (see e.g. Lavoie et al., 2006). Consequently, NiSi was studied extensively at the conditions at which these devices are manufactured and operated, i.e. at ambient conditions (e.g. Connétable & Thomas, 2009) and at high temperatures (e.g. Detavernier et al., 2003), where NiSi has the MnP (B31) structure. In contrast, we are interested in NiSi because of its position as an end-member in the Fe-Ni-Si system, of relevance to the cores of the terrestrial planets, not least that of Earth. Geochemical models based on cosmochemical arguments suggest that Earth's core could contain at least 5 wt.% nickel (e.g. Allègre et al., 1995) and up to 20 wt.% silicon (e.g. Allègre et al. 1995; Fischer et al. 2012; Balchan & Cowan, 1966). Attempts to reconcile experimental measurements of sound velocities with 1-D seismic profiles (Badro et al., 2007) suggest that silicon is an effective candidate for the light element required to explain Earth's core density deficit. More recent *ab initio* determinations of sound velocities in FeSi exclude silicon as an inner core component (Ono et al. 2013). However, this conclusion depends on the temperature at the inner core boundary (ICB) being less than 6500 K, which is within error of current estimates and thus may be in doubt (Anzellini et al., 2013; Sola & Alfè, 2009) and on the absence of any strong pre-melting effects (Martorell et al., 2013). Recent measurements indicating that the silicon of the bulk silicate Earth is isotopically heavy relative to the chondritic meteorites from which Earth is postulated to have formed, lends further credence to the argument for a significant silicon reservoir within the core (Armytage et al., 2011). As a result, several studies have been published concerning the sub-solidus phase relations (e.g. Sakai et al., 2011) and melting behaviour (e.g. Morard et al., 2011) of a range of ternary alloys within the Fe-Ni-Si system. The phase diagram of the FeSi end-member has also been extensively studied (Lord et al. 2010; Santamaría-Pérez & Boehler, 2008; Dobson et al. 2002; Vočadlo et al., 1999; Guyot et al. 1997), as have the physical properties of its

43   constituent phases (e.g. Sata et al. 2010; Dobson et al. 2003; Vočadlo et al., 1999). Recently, we

44   began an ongoing effort to study the NiSi end-member, the behaviour of which was entirely

45   unknown at the high-pressure, high-temperature conditions relevant to the interior of the Earth.

46   These efforts include static *ab initio* simulations that predicted a multitude of new high-pressure

47   phases at 0 K (Vočadlo et al., 2012) and complementary laser-heated diamond anvil cell (LH-DAC)

48   experiments (Lord et al., 2012) in which at least two of these were detected: the ε-FeSi (B20)

49   structure and the CsCl (B2) structure. Both studies also reported equations of state (EoS) for these

50   structures as well as for the room pressure phase, at 0 K (for the *ab initio* study), and 300 K (for the

51   LH-DAC study). A third installment (Wood et al., 2013) reported the discovery of another high-

52   pressure phase, with space group *Pmmn*, in multi-anvil press (MAP) experiments together with *ab*

53   *initio* simulations of this new structure, including a 0 K EoS. The present study, in which the

54   melting curve of NiSi is reported, forms a further part of this ongoing effort; it is accompanied by

55   Dobson et al. (submitted) in which the sub-solidus phase relations of NiSi are described using off-

56   line and *in situ* MAP experiments, in combination with the *in situ* LH-DAC experiments described

57   here.

58   Our primary motivation for studying the NiSi melting curve is to provide vital data for those

59   involved in continuing efforts to produce accurate thermodynamic descriptions of core liquids. The

60   composition of these liquids falls within a multi-component system, and their physical properties

61   can be determined by interpolation from the system end-members if the relevant physical properties

62   of those end-members are known. For example, by using the melting curves and room temperature

63   EoS of the end-members in the Fe-O-S system, Helffrich (2012) and Helffrich & Kaneshima (2010;

64   2004) constructed a thermodynamic model and calculated sound velocities for a range of possible

65   core liquids, and then constrained the composition of the liquid outer core by comparison with

66   seismically determined wave speeds. To make these models more realistic, additional components

67   must be added to the compositional space, with nickel and silicon being the most important. This

68   requires a more extensive database of end-member physical properties, with FeSi and NiSi being of

69   primary importance. For both FeSi and NiSi it is the B2 (CsCl) structured phase that is likely to be

70   relevant at the conditions of the deep Earth (Lord et al., 2012; 2010). The room temperature EoS

71   and melting curve of B2-FeSi (Sata et al., 2010; Lord et al., 2010) and the EoS of B2-NiSi (Lord et

72   al., 2012; Vočadlo et al., 2012) are already known; the melting curve of NiSi is the subject of this

73   study.

74   Additionally, we wanted to determine the effects of nickel on FeSi at the conditions of

75   Earth's core mantle boundary (CMB) region. Solid B2 structured FeSi may well be present within

76   Earth's lowermost mantle (the D″ layer; Lord et al., 2010). All pathways for the formation of FeSi

77   involve the iron-rich alloy of the underlying core, and so, given the expected solid solution between

78   the isostructural NiSi and FeSi phases, we would expect any silicide present to be iron-rich

79   (Fe,Ni)Si in the B2 structure (Lord et al., 2012). Knowing the melting curve for NiSi will give an

80   additional constraint on the stability of this material within D″, which depends on its melting curve

81   being above the geotherm.

82   Finally, this study is a further test of the accuracy of our primary method for determining

83   melting in the LH-DAC, namely the observation of changes in the gradient (i.e. plateaux) of

84   temperature vs. laser power curves. This method has been successfully adopted on a number of

85   occasions (Asanuma et al., 2010; Lord et al., 2010; 2009) but the underlying cause behind the

86   observed plateaux is still poorly understood (Geballe & Jeanloz, 2012) leading to inevitable

87   questions about its reliability. To address this issue, we present here not just off-line LH-DAC

88   melting data using this method, but also *in situ* experiments, in both the LH-DAC and the MAP in

89   which melting can be observed directly from the appearance of liquid diffuse scattering (LDS) in X-

90   ray diffraction (XRD) patterns acquired at simultaneous high-pressure, high-temperature conditions,

91   and even from visual identification of convective motion during *in situ* X-radiography.

92   **2. Methods**

93   This study consists of three sets of NiSi melting experiments. The first (see §2.1) was

94   performed off-line in the LH-DAC at the School of Earth Sciences, University of Bristol. The

95   second (see §2.2) consists of a pair of LH-DAC experiments coupled with *in situ* XRD

96   measurements at beam line ID-27 of the European Synchrotron Radiation Facility (ESRF) in

97   Grenoble, France. The final set (see §2.3) consists of a single MAP experiment, again coupled with

98   *in situ* XRD and X-radiography measurements, at beam line X17B2 of the National Synchrotron

99   Light Source (NSLS), Brookhaven National Laboratory, New York, USA. The NiSi starting

100   material was from the batch used in Lord et al. (2012). Additionally, two off-line experiments at

101   Bristol were performed on an Fe_{85}-Ni_5-Si_{10} alloy (subscripts are in wt. %), from the batch used in

102   Morard et al. (2011).

103

104   *2.1 Off-line LH-DAC melting experiments, University of Bristol*

105   These experiments were performed in Princeton-type symmetric DACs using anvils with

106   200-250 μm diameter culets. Rhenium gaskets were used, pre-indented to 25 GPa and drilled

107   centrally to create a sample chamber ⅓ the diameter of the culet. Between 1 and 5 densified foils

108   (Lord et al., 2012) of the starting material, 10-40 μm in diameter and 5-10 μm thick, were loaded

109   into the sample chamber between discs of NaCl the same diameter as the sample chamber and ~15

110   μm thick. These form-fitting discs, which act as both pressure medium and thermal insulation, were

111   cut using an automated UV (266 nm) laser ablation unit (New Wave Research, LUV series) from

112   sheets produced by compressing powder, either between a pair of diamond anvils or between steel

113   plates in a hydraulic press. Form-fitting pressure media eliminate void space in the sample chamber,

114   helping to maintain the sample geometry during compression. In addition, this ensures a near

115   identical thickness of insulation on either side of the sample, which makes equalizing the

116   temperatures on the two sides by varying the laser power significantly easier. Several sub-micron

117    $Cr:Al_2O_3$ (ruby) grains were placed between the sample and NaCl on one side, to allow the pressure

118   to be monitored by ruby fluorescence spectroscopy before and after heating. Each cell was held for

119   1 hour under a N_2 atmosphere at 120°C before being sealed under the same conditions to remove

120   any adsorbed water.

121   Once at pressure, samples were heated in a double-sided geometry using two 100 W diode

122   pumped TEM_{00} (Gaussian mode) fiber lasers (model R4, SPI lasers Ltd., Southampton, UK)

123   operating at 1070 nm. If used in their raw state, the Gaussian energy distribution of the lasers

124   inevitably results in strong Gaussian temperature gradients on the sample surface (Fig. 1) that can

125   lead to overestimates of temperature when measured using spectroradiometry due to chromatic

126   aberration imparted by the refractive optics (Walter & Koga, 2004). Furthermore, strong

127   temperature gradients increase the sensitivity of the measured temperature to misalignment of the

128   emitted light with the aperture of the spectrometer and so can result in underestimates of

129   temperature. Finally, they can promote thermally induced (Soret) diffusion in the sample (Sinmyo

130   & Hirose et al., 2010). To minimize these problems, we have employed beam-shaping optics

131   (focal-πShaper, AdlOptica, Berlin, Germany), which convert the Gaussian energy distribution into a

132   distribution with a flat-topped profile (Fig. 1; Prakapenka et al., 2008). Subsequent variable beam

133   expansion optics (model 56-30-2-8X, Special Optics Inc., New Jersey, USA) allow the diameter of

134   the spot to be varied up to ~30 μm.

135   Long working distance infinity-corrected apochromatic near infra-red objective lenses (M

136   Plan Apo NIR 10x, Mitutoyo) were employed to focus the laser light onto and collect the

137   incandescent light from the sample. These lenses absorb a small proportion of the IR radiation

138   causing them to heat up, flex, and change their focal length. Consequently we have found it

139   necessary to water cool the lenses as well as the LH-DAC. These lenses significantly reduce

140   chromatic aberration compared to the optics used in previous studies (Fig. 2a; Lord et al. 2010;

141   2009). As a result, it is no longer necessary to eliminate the most aberrant non-paraxial rays using f-

142   stops, thus making temperature measurement feasible at lower temperatures (down to 1400 K).

143   While the shorter focal length of these objectives increases the magnification (50x vs. 20x

144   previously) and ideal system resolution (0.5 μm vs. 1.25 μm previously), the system is diffraction

145   limited to 1.0 – 1.5 μm across the spectral range available for temperature fitting (570 – 840 nm).

146   This is confirmed by measurement of the width of a sharp interface focused onto the CCD, which

147   indicates an actual resolution of ~1 μm. Optical aberrations, especially of the chromatic variety,

148   reduce the effective spectroradiometric resolution further (Walter and Koga, 2004). On the basis of

149   the measured focal deviations of our system (a maximum of ~10 μm at the image plane over the

150   200 nm spectral window used for temperature fitting), we calculate an actual system temperature

151   measurement resolution of ~3 μm at the sample surface (object plane). Thus, a temperature

152   calculated from the spectrum recorded by a single row of the CCD (e.g. every 0.5 μm at the object

153   plane), must be viewed as a temperature representing an integration of light from a ~9 μm^2 region.

154   This integration will lead to errors in the measured temperature that are a function of the

155   temperature gradient at the sample surface (Walter and Koga, 2004), minimized in this study by the

156   use of beam-shaping optics. The degree of chromatic aberration is reflected in the precision of the

157   spectral fits to the ideal greybody Wien function (Fig. 2a; Walter & Koga, 2004), which in the case

158   of this study was typically 2-5K (Fig. 1 and 2b), a significant improvement over the 3-13K reported

159   previously (Lord et al. 2010). All things considered, we conservatively estimate the error associated

160   with optical aberrations at less than 50 K. As in our previous publications, we do not attempt to

161   assign uncertainties due to the unknown emissivity of the sample. Ambient pressure calibration

162   experiments on a range of metals indicate that this uncertainty does not exceed 200 K (Lord et al.

163   2010; 2009).

164   To minimize uncertainties due to radial pressure gradients, pressures were measured after

165   heating as close as possible to the location of melting. No correction for the effects of thermal

166   pressure can be made to the off-line melting data (cf. §2.2) because we have insufficient *in situ* data

167   to accurately determine the empirical relationship between the thermal pressure and the factors that

168   control its magnitude. These include the specific geometry of each assembly, the physical properties

169   of the sample and pressure medium (both of which undergo phase transitions within the range of

170   our data), the degree of compression and the melting temperature (e.g. Errandonea et al. 2003). The

171   *in situ* experiments (§2.2) indicate maximum thermal pressures of 6 GPa. The resulting

172   overestimate in the melting temperature never exceeds ~200 K, is <100 K by ~60 GPa and becomes

173   insignificant at the pressures relevant to the deep Earth.

174   We use the ruby pressure scale of Dewaele et al. (2008), which falls approximately in the

175   middle of several recent calibrations, with a range of ~4 GPa at 100 GPa (see their Fig. 4a); we add

176   an uncertainty to our pressure measurements encompassing this range. Additional uncertainty terms

177   of ±0.5-1.0 GPa (to take account of radial pressure gradients) and ±0.2 GPa (the analytical error on

178   the position of the R_1 ruby fluorescence line) are also included.

179

180   *2.2 In situ LH-DAC melting experiments, ESRF*

181   Sample assemblies were identical to those used off-line (§2.1), except that no ruby grains

182   were placed in the sample chamber, to simplify XRD analysis. Instead, pressure was monitored

183   using the measured unit cell volumes of NaCl, in either the B1 or B2 structures, and their known

184   thermal EoS (Dorogokupets & Dewaele, 2007). The total pressure at high temperature was

185   determined using the method of Campbell et al. (2009). However, to ensure comparability between

186   all datasets, the melting pressures reported in Table 1 for the *in situ* data are also post-heating

187   pressures determined at room temperature.

188   Laser heating was performed using a double-sided, off-axis geometry with heated spots 20-

189   30 μm in diameter. The incandescent light from the sample was collected using reflective optics

190   while a 2 x 2 μm area centered on the heated spot was selected using a pinhole and analysed

191   spectroradiometrically to determine the sample temperature. Temperatures were measured on both

192   sides of the sample before the start of the experiment to allow the temperatures to be equalized by

193   varying the laser power, but on the upstream side only during the melting run due to the necessity of

194   removing the light collecting optics from the path of the diffracted X-rays. For further details see

195   Schultz et al. (2005).

196   The 3×3 μm X-ray beam ($\lambda = 0.3738$ Å) was co-aligned with the laser-heated spot using

197   the X-ray induced fluorescence of the NaCl pressure medium. Diffracted X-rays were collected on

198   a MAR345 CCD with exposure times of 2-10 seconds. The distance between the sample and

199   detector was calibrated using a LaB_6 standard. For further details of the beam-line see Mezouar et

200   al. (2005). The resulting 2-D diffraction patterns were carefully masked to remove any saturated

201   spots and then integrated into 1-D diffraction patterns using the Fit2D program (Hammersley,

202   1997). The 1-D patterns were in turn fitted and analysed using the Le Bail method (Le Bail *et al.*,

203   1988) as implemented in the GSAS suite of programs (Larson & Von Dreele, 2000; Toby, 2001).

204

205 *2.3 In situ MAP melting experiment, NSLS*

206   This experiment was performed in a cubic DIA type apparatus. The cylindrical sample

207 chamber contained three compartments, separated with Re foil, the first containing NiSi, the second

208 an NaCl + BN pressure standard with a 10:1 ratio by weight and the third containing a mixture of

209 elemental nickel and silicon in a 1:1 atomic ratio. The sample was surrounded by a BN sleeve,

210 followed by a cylindrical graphite heater separated from the 6 mm pyrophyllite cube with an Al_2O_3

211 sleeve. A D-type thermocouple (W/3 % Re-W/25 % Re) was inserted through the furnace and BN

212 sleeve, with the contact just inside the pressure standard.

213   The sample was compressed at room temperature to an end load of 70 tons (a sample

214 pressure of 7 GPa) and then heated in increments of 50-100 K up to 1523 K. At each step, all three

215 samples were analysed using an incident white X-ray beam with a diameter of 50 μm. The

216 diffracted X-rays were collected using a 10 element energy-dispersive detector (Weidner et al.

217 2010) with a 2θ angle of ~6.6° calibrated using the diffraction pattern of Al_2O_3 recorded at 1

218 atmosphere. By widening the slits collimating the incident X-ray beam, radiographic images were

219 recorded regularly to monitor sample geometry. Once melting was determined from the appearance

220 of LDS, this imaging mode was used to produce X-ray videography of the sample at 10 frames per

221 second to monitor the sample for evidence of convection.

222

223 *2.4 Melt detection*

224   In the *in situ* MAP and LH-DAC melting experiments, the appearance of LDS during XRD

225 was the primary melting criterion. In the off-line LH-DAC experiments however, melting was

226 detected by the appearance of plateaux in the laser power vs. temperature function (Figs. 2c, 3, and

227 9) generated during automated linear incremental ramping of the power to the lasers, coupled with

228 regular temperature measurements (also automated). Lord et al. (2009) suggested that plateaux

229 would be expected at any invariant melting point as the laser power provides the latent heat of

230   melting. However, it has since been suggested that this explanation of the observed plateaux is

231   unlikely because the magnitude of the latent heat involved in the melting of such small samples is

232   dwarfed by the heat provided by the laser (Geballe & Jeanloz, 2012; Lord et al, 2010). It is likely

233   that several factors contribute to the observed thermal perturbations, including differences in the

234   optical and thermal properties of the liquid and solid phases. For example, convection in the liquid

235   rapidly moves excess heat from the melt pool (upon which the laser is incident) to the solid/liquid

236   boundary, where it promotes further melting, thus moving the boundary further away from the

237   center of the heated spot without significantly increasing the temperature. This process continues

238   until the whole sample is molten or, more likely, until the boundary is sufficiently far from the

239   incident laser beam that any additional power is lost by conduction to the surroundings rather than

240   promoting further melting. At this point, the molten part of the sample often becomes super-

241   liquidus, its temperature rising linearly with increasing laser power, until a second plateaux is

242   reached, often within error of the known melting curve of the surrounding NaCl pressure medium

243   (Fig. 3a; Boehler et al., 1997). Alternatively, the melt may become mechanically unstable and flow,

244   leading to sudden variations in temperature. Whatever the underlying process, the key point is that

245   this melting criterion has been used to successfully detect melting in a broad range of metallic and

246   intermetallic compounds, including Fe, Pt, Pb, FeS, Fe_3C, Fe_7C_3, the $Fe-Fe_3C$ eutectic (Lord et al.

247   2009) and FeSi (Lord et al. 2010). All of these data either match closely with LH-DAC melting

248   data, published by other research groups and produced using a range of different melting criteria

249   (Fe, Pt, Pb, FeS, FeSi) including *in situ* XRD (Fe, Pb, FeSi) or have been corroborated at low

250   pressures using large volume press (LVP) apparatus based on *ex situ* textural analysis (Fe_3C, Fe_7C_3,

251   the $Fe-Fe_3C$ eutectic and FeSi; see Lord et al., 2010; 2009 and references therein). The present

252   study provides two additions to this list: firstly, the melting curve of NiSi corroborated using *in situ*

253   XRD in both the LH-DAC and the MAP and secondly, two offline melting experiments on an Fe_{85}-

254   Ni_5-Si_{10} alloy, for which *in situ* melting data already exist (Morard et al. 2011).

255   In the case of the off-line experiments, the uncertainties in the melting temperatures reported

256   here are a sum of: 1) the analytical precision in the blackbody spectral fitting (typically ±2-5 K; see

257   §2.2); 2) the standard deviation of the temperatures within the melting plateau (typically ±50-150

258   K); and 3) an additional estimate of the temperature variations within the central part of the hotspot

259   from which the temperature is determined (typically ±25-50 K; see Fig. 1a) leading to total

260   uncertainties of ±80-200 K. In the case of the *in situ* experiments, the reported uncertainties are

261   simply chosen to encompass the temperatures of the two XRD analyses that bracket the appearance

262   of LDS plus the maximum estimated uncertainty in the temperature measurements (±150 K; e.g.

263   Morard et al. 2011).

264   **3. Results**

265   The NiSi data are listed in Table 1, and plotted as a function of pressure in Fig. 4a, and as a

266   function of isothermal compression, relative to the ambient pressure volume of B31-NiSi in Fig. 5.

267   At ambient pressure, NiSi melts congruently from the MnP (B31) structure but undergoes a

268   series of solid-state phase transitions with increasing pressure. The next liquidus phase on increase

269   in pressure has the ε-FeSi (B20) structure, with the transition initially bracketed at 12.5±4.5 GPa

270   and 1550±150 K on the basis of the XRD analysis of LH-DAC experiments (Lord et al. 2012). The

271   Clapeyron slope of this transition has since been refined from the XRD analysis of off-line MAP

272   experiments (Fig. 4a; Dobson et al. submitted). All melting data below this transition have been

273   fitted separately, using two methods. Firstly, the *P-T* data (Fig. 4a) are fitted using the Simon-

274   Glatzel equation $T_m = [(P_m/A + 1)]^{1/C} \times T_0$, where T_m is the melting temperature at pressure P_m,

275   T_0 is the ambient pressure melting point and *A* and *C* are fitting parameters (Simon & Glatzel, 1929;

276   see Table 2). Secondly, the melting temperatures are plotted as a function of isothermal

277   compression, $(V_0 - V)/V_0$, using the EoS for B31-NiSi (Lord et al., 2012) and fitted using the

278   Kraut-Kennedy equation $T_m = T_0(1 + C(V_0 - V)/V_0)$ where V_0 is the ambient pressure volume of

279   B31-NiSi, and V is the volume of the liquidus phase at the pressure of melting (Fig. 5; Kraut &

280   Kennedy, 1966). This approach is justified because the data are linear in *T* vs. $(V_0 - V)/V_0$ space.

281   Both fits pass within error of the off-line LH-DAC data and the single *in situ* MAP melting point at

282   5.5 GPa. In the latter experiment melting was not only detected by the onset of LDS in the XRD

283   patterns, but is also clearly demonstrated by the appearance of convective motion in an X-

284   radiographic video acquired after the onset of LDS (see Supplementary video). The invariant point

285   at which our newly determined B31-NiSi liquidus intersects the B31 → B20 transition line (Dobson

286   et al., submitted) defines the B31 + B20 + L triple point (TP1; 12±2 GPa, 1550±100 K).

287   Fig. 6 shows the first of the *in situ* LH-DAC experiments at the ESRF (experiment 31A)

288   while Fig. 7 shows selected diffraction patterns. Before heating the sample consists of pure B31-

289   NiSi (Fig. 7a). Up to 1700 K the assemblage consists of B20-NiSi plus the orthorhombic *Pmmn*

290   phase (Fig. 6a and 7b; Wood et al., 2013) which are known to share a broad two-phase region. The

291   *Pmmn* phase has been found to be stable above a pressure of ~13 GPa and below a temperature of

292   ~1100 K (Dobson et al., submitted). At a constant laser output of 26.5% the temperature of the

293   sample rose from 1650 K to 1850 K, during which time the *Pmmn* phase disappeared, leaving B20-

294   NiSi plus several, small, unidentified peaks (Fig. 7c). From this point up to 29% laser power these

295   unidentified peaks diminish in both number and intensity, while temperature increases linearly,

296   followed by a sudden jump and then a plateau that yields a melting temperature of 2180±30 K. At

297   30% laser power, while on the plateau, LDS was observed during XRD (Fig. 6b), with the

298   magnitude of the LDS signal increasing as laser power is increased while the temperature remains

299   approximately constant. In this experiment, the B2-NiSi phase appeared simultaneously with the

300   onset of melting, suggesting that this run fortuitously intersected the B20 + B2 + L triple point

301   (TP2). After heating (Fig. 7d), the quenched assemblage consists of B20-NiSi + B2-NiSi while two

302   of the unidentified peaks, both very small, persist. Given that the integrated area under these peaks

303   is only 0.8% that of the peaks from the indexed NiSi phases, we are confident that the molten

304   system is close to the NiSi stoichiometry. Nevertheless, a detailed discussion of the nature of these

305   peaks can be found in the supplementary material. Using the post-heating pressure for this run, the

306   triple point is thus defined as 28.5±1.3 GPa and 2165±61 K.

307   The melting data that fall within the narrow pressure range where B20-NiSi is the liquidus

308   phase, between TP1 and TP2, were too few to fit. Instead, we have opted to connect the two triple

309   points with a slightly convex upward curve in *P-T* space to prevent Schreinemaker's rules being

310   contravened (Fig. 4a; Zen, 1966) and by a straight line in *V-T* space (Fig. 5).

311   The melting data above TP2 have also been fitted separately using the Simon-Glatzel and

312   Kraut-Kennedy equations (Table 2). In this case the Simon-Glatzel equation has been modified

313   such that $T_m = [((P_m - 28.5)/A + 1)]^{1/C} \times T_0$ in order to force the melting curve through the triple

314   point. The Kraut-Kennedy equation is also modified, such that $T_m = T_0[1 + (C(V_0 - V)/V_0) -$

315      $0.104557)]$.

316   The pair of off-line melting experiments performed on Fe_{85}-Ni_5-Si_{10} are presented as a

317   function of pressure in Fig. 8 with the raw data in Fig. 9. Both points fall within error of the melting

318   curve of Morard et al. (2011), which is defined by two brackets determined from the appearance of

319   LDS in *in situ* LH-DAC experiments. Our data also agree with those of Fischer et al. (2013) on a

320   similar composition ($Fe_{91}Si_9$) in which both LDS and plateaux in temperature vs. laser power

321   functions were used as melting criteria.

322

4. Discussion & conclusions

4.1 The NiSi phase diagram

The data reported here and in Dobson et al. (submitted) provide additional constraints on the

NiSi phase diagram, including the melting curves of all three liquidus phases (B31, B20, B2) and

the positions of both triple points. It is clear from Figs. 4a and 5 that the inflection associated with

TP1 is much larger than that associated with TP2. This is probably related to the fact that the

volume change across the B31 → B20 transition (-6%) is significantly larger than that across the

B20 → B2 transition (-0.8%) as is clear from Fig. 5. Although there are insufficient data to

determine the liquidus for B20-NiSi by fitting, the constraints on the two triple points are

independent and thus the slope is tightly constrained, and clearly significantly steeper than that of

B31-NiSi, but similar to that of B2-NiSi (Fig. 5).

The *in situ* LH-DAC experiments allow us to refine our estimate of the Clapeyron slope of

the B20 → B2 transition. Our initial estimate of ~-105 MPa K^{-1} was based on an experimental

bracket at 46±3 GPa and 1900±150 K (Lord et al., 2012) and a prior *ab initio* study (Vočadlo et al.,

2012) which determined that B2-NiSi would become stable relative to the preceding Pnma-II

structure at 247 GPa and 0 K. Wood et al. (2013) have since shown that at 0 K the B2 structure

becomes stable at 264 GPa, from the newly discovered Pmmn structure. However, if we use the

more relevant B20 → B2 transition pressure of 170.5 GPa at 0 K from Vočadlo et al. (2012), the

Clapeyron slope decreases to ~-67 MPa K^{-1}. The new *in situ* data (TP2 plus an additional bracket at

1715±35 K and 58.5±1 GPa from the second of the two experiments) yield an identical value

(Dobson et al., submitted). This new slope passes within the bracket reported by Lord et al. (2012)

and extrapolates to 173 GPa at 0 K, in excellent agreement with the 0 K B20 → B2 transition

pressure of 170.5 GPa from Vočadlo et al. (2012). This new estimate is preferred because the

previous estimate was constructed assuming a linear boundary between the pressure at which the

347   B2 phase becomes stable at 0 K and the experimental value from Lord et al. (2012); in fact there are

348   likely to be additional phase boundaries in between, leading to inflections in the transition to the B2

349   phase (Dobson et al., submitted). This explains the difference between the 0 K stabilization pressure

350   of B2-NiSi predicted by the *ab initio* simulations (264 GPa; Wood et al., 2013) and the pressure that

351   would be expected from a linear extrapolation of the experimentally determined Clapeyron slope

352   (173 GPa). This new value confirms that the B2 structure is the relevant one for NiSi at Earth's core

353   conditions given that no further phase transitions are expected at higher pressures (Wood et al.,

354   2013; Vočadlo et al., 2012).

355

356   *4.2 Comparison with FeSi*

357   The NiSi phase diagram has two significant differences from the phase diagram of FeSi

358   (Lord et al., 2010). Firstly, it exhibits a greater degree of polymorphism at pressures and

359   temperatures below the B20 → B2 transition, with at least two additional stable phases (B31 and

360   *Pmmn*) and perhaps several more (Wood et al., 2013; Lord et al., 2012; Vočadlo et al., 2012).

361   Secondly, its liquidus is considerably lower in temperature, by 425 K at 1 atmosphere and by a

362   maximum of ~900 K at 12 GPa (TP1). On the other hand, the B20 → B2 transition, shared by both

363   compositions, involves a very similar reduction in volume (0.8% for NiSi vs. 1.1% for FeSi, at 300

364   K; Lord et al., 2012) and has a very similar Clapeyron slope (-67 MPa K^{-1} for NiSi compared to -56

365   MPa K^{-1} for FeSi; Lord et al., 2010). In fact if the FeSi phase diagram were shifted in pressure such

366   that the B20 + B2 + L triple points for both compositions coincided, the B2 liquidus and B20 → B2

367   transitions would be almost indistinguishable (Fig. 4a). However, the more recent *in situ* FeSi phase

368   diagram (Fischer et al., 2013) contradicts this conclusion (see their Fig. 1d). In that study, a two-

369   phase loop was observed in which the assemblage B20 + B2 is stable (the compositions of which

370   must be non-stoichiometric but complementary), followed by a near vertical transition at 40 GPa to

371   single phase, B2-FeSi. Presumably this two-phase region is bounded at lower pressures by a

372   transition to single-phase B20-FeSi at a pressure below the lower limit of their experiments.

373   Looking at the phase diagram presented in Fig. 2 of Lord et al. (2010), this interpretation could

374   explain the majority of the data. Although the results of *ex situ* MAP synthesis experiments

375   published by Dobson et al. (2002), in which pure B2-FeSi was observed at 24 GPa and 2023 K,

376   appear to contradict this new interpretation, those experiments purposefully used non-stoichiometric

377   starting material ($Fe_{52}Si_{48}$). This slight metal excess is known to stabilize the B2 structure in both

378   FeSi and RuSi (Dobson et al., 2002) and might explain its appearance at lower pressures in the

379   MAP experiments. However, it seems unlikely that an iron excess of 2% could reduce the pressure

380   at which B2-FeSi becomes the sole polymorph by such a large extent (18 GPa). Furthermore,

381   Dobson et al. (2002) found that at 24 GPa the width of the two-phase loop is less than 4 wt. % (i.e.

382   pure B20 at $Fe_{48}Si_{52}$ and pure B2 at $Fe_{52}Si_{48}$), which is hard to reconcile with the width of 28 GPa in

383   pressure space reported by Fischer et al. (2013). In light of this contradiction, we have chosen to

384   present both of the proposed boundaries in Fig. 4.

385   It has been predicted that FeSi could be present within the D″ region, either as a reaction

386   product between the $(Mg,Fe)SiO_3$ perovskite or post-perovskite of the lower mantle and the Fe-Ni

387   alloy of the outer core (Knittle & Jeanloz, 1991) or as a result of exsolution from the core during

388   secular cooling (Buffett et al., 2000). Based on its melting curve and estimates of the geotherm

389   within the D″ region (Lord et al., 2010), it is expected that any FeSi present would be solid at the

390   top of the D″ region, but almost certainly molten toward the bottom (with the depth of the transition

391   dependent on the geotherm), making it a potential candidate for a component of the partial melts

392   postulated to explain the seismic ultra-low velocity zones (ULVZs) observed at the CMB (e.g.

393   Idehara, 2011; Buffett et al., 2000). A recent *in situ* XRD study on FeSi confirms that the B2

394   structure is stable to at least 150 GPa and 2200 K (Fischer et al., 2013) while no further phase

395   transitions are expected in NiSi on the basis of extensive *ab initio* simulations on a range of possible

396   polymorphs (Wood et al., 2013; Vočadlo et al., 2012). FeSi and NiSi are therefore likely to be

397   isostructural at CMB conditions probably forming the end-members of a simple binary solid

398   solution. Given this assumption and that the core contains at least 5 wt.% Ni (e.g. Allègre et al.,

399   1995), any silicide produced would be expected to be B2 structured (Fe,Ni)Si, with a liquidus

400   temperature falling somewhere between the two end-members. If we extrapolate our Simon-Glatzel

401   fit of the B2-NiSi melting data to the CMB pressure of 135 GPa we find an NiSi melting

402   temperature of 3700±400 K, well within error of the value for FeSi of 4000±200 K (Lord et al.

403   2012). Employing our Kraut-Kennedy fit yields essentially the same result. Combined with the fact

404   that any (Fe,Ni)Si phase is likely to be iron-rich, largely reflecting the composition of the core, the

405   present results strongly indicate that the incorporation of Ni has little effect on the conclusions

406   discussed in Lord et al. (2010).

407   The present data do not cover a sufficient pressure range to allow a reliable extrapolation of

408   the NiSi melting curve to ICB conditions (330 GPa). The likelihood that FeSi and NiSi will be

409   isostructural at inner core conditions means that the melting temperature of any iron-rich B2

410   structured (Fe,Ni)Si phase at the ICB pressure of 330 GPa is likely to be only slightly lower than

411   the value of 6200 K determined for FeSi (Lord et al., 2010). Consequently, such a phase could be a

412   stable solid at inner-core conditions, given favorable sub-solidus phase relations in the Fe-Ni-Si

413   system, which are largely unknown at these conditions. However, most recent experimental data

414   (Fischer et al., 2013; Brosh et al., 2009) and *ab initio* simulations (Zhang & Oganov, 2010) in the

415   Fe-Si system suggest that if the inner core contains more than 4 wt. % Si, as predicted by most

416   experimental and modeling studies (e.g. Allègre et al. 1995; Fischer et al. 2012; Balchan & Cowan,

417   1966) an assemblage of hcp + B2 structures will be stabilized. These results contradict earlier

418   experimental studies (e.g. Asanuma et al., 2008; Kuwayama et al., 2009) which suggested that such

419   bulk compositions would stabilize a single, hcp-structured alloy phase. An alternative inner core

420   model containing 1-2 wt.% Si and 4-5 wt.% Ni, based on sound velocity measurements, has been

421   proposed by Antonangeli et al. (2010). In this case, the phase diagram proposed by Fischer et al.

422   (2013) would also predict a single phase, hcp-structured inner core.

423

424   *4.3 Melting criteria*

425   The data described here provide additional evidence that plateaux in temperature vs. laser

426   power curves are a reliable proxy for melting in those materials that we have tested to date. The

427   close correspondence between the MAP experiment and LH-DAC experiments suggests that our

428   spectroradiometric temperature measurements are accurate and that the temperature gradients

429   within our LH-DAC experiments, minimized by beam shaping, are not an issue. This is because, in

430   the MAP experiment, temperature was measured directly using a thermocouple while the

431   temperature gradient is expected to be small due to the external heating geometry.

432   The *in situ* LH-DAC experiments are particularly informative, because they afford us the

433   opportunity to measure the temperature vs. laser power function simultaneously with an

434   independent and direct determination of the melting temperature from the appearance of LDS. In

435   run 31A (Fig. 6a) LDS does not appear until some way into the plateau, either because there is too

436   little liquid within the diffracted volume to produce a visible signal, or because of slight

437   misalignments between the laser heated spot and the X-ray beam. Once the LDS signal appears,

438   however, its magnitude increases with increasing laser power while the temperature remains

439   constant, which strongly suggests that the additional power is causing an increase in the volume of

440   melt rather than increasing the temperature. This behaviour is to be expected given the axial

441   temperature gradients within the sample (likely less than 100 K; see Campbell et al. 2009). The

442   melt volume appears to reach a maximum by 33% laser output and in the next measurement, at

443   34%, the temperature has risen above the plateau, suggesting that the sample was fully molten

444   within the laser-heated volume and that the additional laser power was forcing the melt into the

445   super-liquidus region, but the experiment was halted before this relationship had become

446   convincing. The observation that LDS is coincidental with a plateau in the temperature vs. laser

447   power function confirms that the observed plateaux are the result of progressively increasing melt

448   volumes rather than of sub-solidus transitions.

449   The jump in temperature at the onset of the melting plateau (indicated by the arrow in Fig.

450   6a), sometimes observed (cf. Fig. 2c), may be the result of the difference in emissivity or laser

451   absorption between the solid and liquid phase. Similar behaviour has been observed in an $Fe_{82}Si_{18}$

452   alloy (see Fig. 1 of Asanuma et al., 2010), but not in FeSi (see Fig. 1 of Lord et al. 2010). Given

453   these inconsistencies, no definitive explanation of this behaviour can yet be made.

454   The good agreement between the published *in situ* melting curves of $Fe_{85}Ni_5Si_{10}$ (Morard et

455   al., 2011) and $Fe_{91}Si_9$ (Fischer et al. 2013) and the two off-line melting points on $Fe_{85}Ni_5Si_{10}$

456   reported here indicates that the correspondence between the *in situ* and off-line measurements on

457   NiSi is not a material-specific coincidence. Visual inspection of samples after laser heating provides

458   an additional, secondary, melting criterion. Fig. 9c shows a photomicrograph of experiment 41

459   (sample $Fe_{85}Ni_5Si_{10}$) after laser heating. The two dark spots at the bottom and top right of the

460   sample foil were observed to have formed at the locations of melting runs 41A and 41B

461   respectively. A third heating cycle in which a temperature of 2000 K was maintained for 10 minutes

462   (the white circle in Fig. 9c) produced no change in the sample surface compared to adjacent

463   unheated regions. The exact cause of this discoloration is not known, but it is unlikely to be the

464   result of reaction between the sample and its environment, given the lack of evidence of carbides or

465   other extraneous compounds in diffraction patterns collected on quenched samples of various

466   compositions (Fig. 7d; Lord et al., 2010).

467   Further examples of the reliability of discontinuities in temperature vs. laser power curves as

468   a melting criterion are provided by two recent studies performed by independent groups. Firstly,

469   Fisher et al. (2013) report melting data for $Fe_{91}Si_9$ based on the appearance of LDS during *in situ*

470   XRD. At 88 GPa (3648±149 K) and 101 GPa (3662±224 K), the appearance of LDS coincides with

471   clear plateaux in temperature vs. laser power curves (see their Fig. 4). Fischer et al. (2013) also

472   report a single *in situ* melting bracket for FeSi that closely matches our previously published off-

473   line melting curve (Fig. 4b; Lord et al. 2010) but is ~600 K above the melting curve of Santamaría-

474   Pérez & Boehler (2008) in which melting was determined from visual observations of changes in

475   laser speckle patterns. The second example comes from the new melting curve for iron reported by

476   Anzellini et al. (2013). In Fig. 1c of their paper the authors report a clear example of a discontinuity

477   in the rate of change in temperature as a function of time (equivalent to power given the linear ramp

478   rate) at 4100 K. This matches exactly their LDS based melting curve. Anzellini et al. (2013) note

479   that discontinuities in their temperature vs. power curves are not always apparent (as in their Fig.

480   1d), but that this non-appearance is associated with thicker samples. These two examples indicate

481   that although it is preferable to determine melting curves from the appearance of LDS during *in situ*

482   XRD, in lieu of such data, discontinuities in temperature vs. laser power curves are a useful and

483   accurate alternative approach. In contrast, Anzellini et al. (2013) make clear that earlier

484   measurements of the iron melting curve based on visual observations of motion in laser speckle

485   patterns presumed to represent convection in the liquid considerably underestimated the iron

486   melting curve, as was also the case for FeSi (described above). Anzellini et al. (2013) suggest that

487   these visual methods can potentially misidentify dynamic recrystallization in the solid as melt

488   convection. Therefore it appears that plateaux in temperature vs. laser power curves provide the

489   more accurate criterion in off-line melting experiments.

Acknowledgements

References

Allègre CJ, Poirier J-P, Humler E, Hofmann AW (1995) The chemical composition of the Earth.
    Earth Planet Sci Lett 134:515-526

Antonangeli D, Siebert J, Badro J, Farber DL, Fiquet G, Morard G, Ryerson FJ (2010) Composition
    of the Earth's inner core from high-pressure sound velocity measurements in Fe–Ni–Si
    alloys. Earth Planet Sci Lett 295:292–296

Anzellini S, Dewaele A, Mezouar M, Loubeyre P, Morard G (2013) Melting of Iron at Earth's
    Inner Core Boundary Based on Fast X-ray Diffraction. Science 340:464-466

Armytage RMG, Georg RB, Savage PS, Williams HM, Halliday AN (2011) Silicon isotopes in
    meteorites and planetary core formation. Geochim Cosmochim Acta 75:3662-3676

Asanuma H, Ohtani E, Sakai T, Terasaki H, Kamada S, Kondo T, Kikegawa T (2010) Melting of
    iron–silicon alloy up to the core–mantle boundary pressure: implications to the thermal
    structure of the Earth's core. Phys Chem Minerals. doi: 10 1007/s00269-009-0338-7

Badro J, Fiquet G, Guyot F, Gregoryanz E, Occelli F, Antonangeli D, d'Astuto M (2007) Effect of
    light elements on the sound velocities in solid iron: Implications for the composition of
    Earth's core. Earth Planet Sci Lett 254:233-238.

Balchan AS, Cowan GR, (1966) Shock compression of two iron–silicon alloys to 2.7 megabars. J
    Geophys Res 71:3577–3588

Boehler R, Ross M, Broecker DB (1997) Melting of LiF and NaCl to 1 Mbar: Systematics of Ionic
    Solids at Extreme Conditions. Phys Rev Lett 78:4589-4592

Brosh E, Makov G, Shneck RZ (2009) Thermodynamic analysis of high-pressure phase equilibria
    in Fe–Si alloys, implications for the inner-core. Phys Earth Planet Inter 172:289–298

Buffett BA, Garnero EJ, Jeanloz R (2000) Sediments at the Top of Earth's Core. Science 290:1338-
    1342

530   Campbell AJ, Danielson L, Righter K, Seagle CT, Wang Y, Prakapenka VB (2009) High pressure

531   effects on the iron–iron oxide and nickel–nickel oxide oxygen fugacity buffers. Earth Planet

532   Sci Lett 286:556-564

533   Connétable D, Thomas O (2009) First-principles study of the structural, electronic, vibrational, and

534   elastic properties of orthorhombic NiSi. Phys Rev B 79:094101

535   Detavernier C, Lavoie C, d'Heurle FM (2003) Thermal expansion of the isostructural PtSi and

536   NiSi: Negative expansion coefficient in NiSi and stress effects in thin films. J Appl Phys

537   93:2510-2515

538   Dobson DP, Hunt SA, Ahmed J, Lord OT, Wann ETH, Santangeli J, Wood IG, Vočadlo L, Walker

539   A, Mueller HJ, Lathe C, Whitaker M (submitted) The phase diagram of NiSi to 19 GPa and

540   preliminary results to 60 GPa. Phys Earth Planet Inter

541   Dobson DP, Chrichton WA, Bouvier P, Vočadlo L, Wood IG (2003) The equation of state of CsCl-

542   structured FeSi to 40 GPa: Implications for silicon in the Earth's core. Geophys Res Lett

543   30:1014, doi:10.1029/2002GL016228

544   Dobson DP, Vočadlo L, Wood IG (2002) A new high-pressure phase of FeSi. Am Min 87:784-787

545   Dorogokupets PI, Dewaele A (2007) Equations of state of MgO, Au, Pt, NaCl-B1, and NaCl-B2:

546   Internally consistent high-temperature pressure scales. High Pressure Res 27:431-446

547   Errandonea D, Somayazulu M, Häusermann D, Mao H-K (2003) Melting of tantalum at high

548   pressure determined by angle dispersive x-ray diffraction in a double-sided laser-heated

549   diamond-anvil cell. J Phys Condens Matter 15:7635-7649

550   Fischer RA, Campbell AJ, Reaman DM, Miller NA, Heinz DL, Dera P, Prakapenka VB (2013)

551   Phase relations in the Fe–FeSi system at high pressures and temperatures. Earth Planet Sci

552   Lett 373:54-64

553   Fischer RA, Campbell AJ, Caracas R, Reaman DM, Dera P, Prakapenka VB (2012) Equation of

554   state and phase diagram of Fe–16Si alloy as a candidate component of Earth's core Earth

555   Planet Sci Lett 357–358:268–276

556   Idehara K (2011) Structural heterogeneity of an ultra-low-velocity zone beneath the Philippine

557   Islands: Implications for core–mantle chemical interactions induced by massive partial

558   melting at the bottom of the mantle. Phys Earth Planet Sci 184:80-90

559   Geballe Z, Jeanloz R, (2012) Origin of temperature plateaus in laser-heated diamond anvil cell

560   experiments. J App Phys. doi: 10.1063/1.4729905

561   Guyot F, Zhang JH, Martinez I, Matas J, Ricard Y, Javoy M (1997) P-V-T measurements of iron

562   silicide (epsilon-FeSi). Implications for silicate-metal interactions in the early Earth. Eur J Min

563   9:277-285

564   Hammersley AP (1997) FIT2D: an introduction and overview. ESRF Technical Report ESRF-97-

565   HA-02T, Grenoble, France

566   Helffrich G (2011) How light element addition can lower core liquid wave speeds. Geophys J Int

567   doi:10.1111/j.1365-246X.2011.05295.x

568   Helffrich G, Kaneshima S (2010) Outer-core compositional stratification from observed core wave

569   speed profiles. Nature 468:807-810

570   Helffrich G, Kaneshima S (2004) Seismological Constraints on Core Composition from Fe-O-S

571   Liquid Immiscibility. Science 306:2239-2242

572   Hofmeister AM, Mao H-K (2003) Pressure derivatives of shear and bulk moduli from the thermal

573   Grüneisen parameter and volume-pressure data. Geochim Cosmochim Acta 67:1215-1235

574   Knittle E, Jeanloz R (1991) Earth's Core-Mantle Boundary: Results of Experiments at High

575   Pressures and Temperatures. Science 251:1438-1443

576   Kraut EA, Kennedy GC (1966) New melting law at high pressures. Phys Rev Lett 16:608-609

577   Larson AC, Von Dreele RB (1994) General Structure Analysis System (GSAS). Los Alamos

578   National Laboratory Report LAUR 86-748

579   Lavoie C, Detavernier C, Cabral C, d'Heurle FM, Kellock AJ, Jordan-Sweet J, Harper JME (2006)

580   Effects of additive elements on the phase formation and morphological stability of nickel

581   monosilicide films. Microelectron Eng 83:2042-2054

582   Le Bail A, Duroy H, Fourquet JL (1988) Ab-initio structure determination of $LiSbWO_6$ by X-ray

583   powder diffraction. Mater Res Bull 23:447-452

584   Lord OT, Vočadlo L, Wood IG, Dobson DP, Clark SM, Walter MJ (2012) High-pressure phase

585   transitions and equations of state in NiSi. II. Experimental results. J App Cryst 45:726-737

586   Lord OT, Walter MJ, Dobson DP, Armstrong L, Clark SM, Kleppe A (2010) The FeSi phase

587   diagram to 150 GPa. J Geophys Res 115:B06208

588   Lord OT, Walter MJ, Dasgupta R, Walker D, Clark SM (2009) Melting in the Fe–C system to 70

589   GPa. Earth Planet Sci Lett 284:157-167

590   Martorell B, Brodholt J, Wood IG, Vočadlo L (2013) The effect of nickel on the properties of iron

591   at the conditions of Earth's inner core: Ab initio calculations of seismic wave velocities of

592   Fe–Ni alloys. Earth Planet Sci Lett 365:143-151

593   Massalski TB, Subramanian PR, Okamoto H, Kacprzak L (1990) Binary Alloy Phase Diagrams,

594   second ed., ASM International, Materials Park, OH.

595   Morard G, Andrault D, Guignot N, Siebert J, Garbarino G, Antonangeli D (2011) Melting of Fe–

596   Ni–Si and Fe–Ni–S alloys at megabar pressures: implications for the core–mantle boundary

597   temperature. Phys Chem Minerals 38:767-776

598   Prakapenka V, Kubo A, Kuznetsov A, Laskin A, Shkurikhin O, Dera P, Rivers ML, Sutton SR

599   (2008) Advanced flat top laser heating system for high pressure research at GSECARS:

600   application to the melting behavior of germanium. High Pressure Res.

601   doi:10.1080/08957950802050718

602   Sakai T, Ohtani E, Hirao N, Ohishi Y (2011) Stability field of the hcp-structure for Fe, Fe-Ni, and

603   Fe-Ni-Si alloys up to 3 Mbar. Geophys Res Lett 38:L09302

604   Sata N, Hirose K, Shen G, Nakajima Y, Ohishi Y, Hirao N (2010) Compression of FeSi, Fe3C,

605   Fe0.95O, and FeS under the core pressures and implication for light element in the Earth's

606   core. J Geophys Res 115:B09204

607   Santamaría-Pérez D, Boehler R (2008) FeSi melting curve up to 70 GPa. Earth Planet Sci Lett

608   265:743-747

609   Schultz E, Mezouar M, Crichton W, Bauchau S, Blattmann G, Andrault D, Fiquet G, Boehler R,

610   Rambert N, Sitaud B, Loubeyre P (2005) Double-sided laser heating system for *in situ* high

611   pressure–high temperature monochromatic X-ray diffraction at the ESRF. High Pressure

612   Res. doi: 10 1080/08987950500076031

613   Simon F, Glatzel G (1929) Bernerkungen zur Schmelzdruckkurve. Z Anorganische Allgemeine

614   Chem 178:309-316

615   Sinmyo R, Hirose K (2010) The Soret diffusion in laser-heated diamond-anvil cell. Phys Earth

616   Planet Int 180:172-178

617   Sola E, Alfè D (2009) Melting of Iron under Earth's Core Conditions from Diffusion Monte Carlo

618   Free Energy Calculations. Phys Rev Lett 103:078501

619   Toby BH (2001) EXPGUI, a graphical user interface for GSAS. J App Cryst 34:210-213

620   Vočadlo L, Price GD, Wood IG (1999) Crystal structure, compressibility and possible phase

621   transitions in ε-FeSi studied by first-principles pseudopotential calculations. Acta Cryst

622   B55:484-493

623   Vočadlo L, Wood IG, Dobson DP (2012) High-pressure phase transitions and equations of state in

624   NiSi. I. Ab initio simulations. J App Cryst 45:186-196

625   Walter MJ, Koga KT (2004) The effects of chromatic dispersion on temperature measurement in

626   the laser-heated diamond anvil cell. Phys Earth Planet Inter 143-144:541-558

627   Weidner DJ, Vaughan MT, Wang L, Long H, Li L, Dixon NA, Durham WB (2010) Precise stress

628   measurements with white synchrotron x rays. Rev Sci Instrum 81:013903

629   Wood IG, Ahmed J, Dobson DP, Vočadlo L (2013) High-pressure phase transitions and equations

630   of state in NiSi. III. A new high-pressure phase of NiSi. J App Cryst 46:14-24

631   Zen E-A (1966) Construction of Pressure-Temperature Diagrams for Multicomponent Systems after

632   the Method of Schreinemakers - A Geometric Approach. U. S. Geol Surv Bull 1225:1-56

633

Figure Captions

Figure 1:

(a) Temperature cross-sections measured by spectroradiometry across an NiSi sample at 25 GPa.

The beam shaping optics used in the present study produce relatively isothermal conditions over

wide areas (±35 K over 10 μm; blue circles); without them, much larger gradients are created by the

Gaussian energy profile of the laser (red squares).

Figure 2:

Results from experiment 25D at 27 GPa. (a) Thermal emission spectra collected from the left hand

side, plotted as normalized intensity (J) versus normalized wavelength (ω) where $c_1 = 2\hbar c^2$ and

$c_2 = \hbar c/k$ (c, speed of light; $\hbar$, Planck's constant; k, Boltzmann's constant). Each line represents

the spectrum from a point along a transect across the laser heated spot. The straightness of the data

leads to very low fitting errors (1.6 K in this case) and indicates the successful minimization of the

effects of chromatic aberration, which would be manifested as curvature in the data. (b) Selected

temperature cross-sections collected from the left hand side of the sample during the melting

experiment (in this case, the sample is larger than the heated spot) and (c) the resulting temperature

vs. laser power function showing a clear melting plateau on the left side (open circles) and right

side (closed circles). Temperatures in (c) represent the maxima of the cross-sections in (b). The grey

bars represent +/- one standard deviation of the data in the plateau, which is defined by the arrows

in (c). The uncertainty reported in Table 1 is larger than that reported here because it includes

additional terms (see text). All figures are colour coded as a function of laser power.

Figure 3

658   Further examples of melting induced plateaux in temperature vs. laser power functions in NiSi. (a)

659   Experiment 25B at 21 GPa, (b) experiment 40B at 30 GPa, (c) experiment 28C at 42 GPa, (d)

660   experiment 28E at 54 GPa and (e) experiment 29A at 69 GPa. The small kink in (a) at 62 % laser

661   output is due to a slight adjustment made to the positioning of the laser on the right hand side. Open

662   circles: left hand side; filled circles: right hand side; filled square: melting point of NaCl from the

663   melting curve of Boehler et al. (1997).

664

665   **Figure 4**

666   (a) The NiSi phase diagram above 900 K (black lines). Filled circles: off-line LH-DAC melting

667   points (Bristol); open black (grey) triangles: *in situ* LH-DAC melting brackets determined at the

668   ESRF without (with) thermal pressure included; filled triangles: *in situ* MAP melting bracket

669   determined at the NSLS; filled diamonds: B20 → B2 transition bracket from Lord et al. (2012);

670   open diamond: ambient pressure melting point (Massalski et al. 1990). For the *in situ* experiments,

671   the appearance of LDS was the melting criterion, with the downward pointing arrow representing

672   its first appearance and the upward pointing arrow representing the preceding measurement. The

673   solid grey lines and text relate to the FeSi phase diagram of Lord et al. (2010) while the dashed grey

674   line represents the B20 + B2 → B2 transition determined by Fischer et al. (2013). The sub-solidus

675   parts of the NiSi phase diagram reported here are from Dobson et al. (submitted). (b) The FeSi

676   phase diagram. Lines are as in (a) except for the dot-dash line, which indicates the melting curve of

677   Santamaría-Pérez & Boehler (2008). The solid triangles represent the *in situ* melting bracket from

678   Fischer et al. (2013).

679

680   **Figure 5**

681   The same melting data shown in Fig. 4, plotted as a function of isothermal compression ($V_0 -$

682   V)/V_0 where V is the volume of the liquidus phase at the pressure of melting and V_0 is the ambient

683   pressure volume of B31-NiSi (open circles). The horizontal error bars are asymmetric because they

684   include a contribution equivalent to the maximum measured thermal pressure of +6 GPa. Solid lines

685   represent fits to the Kraut-Kennedy equation for, from left to right, B31-NiSi (red), B20-NiSi

686   (green) and B2-NiSi (blue). The solid circles represent the two triple points, each of which appears

687   twice because of differences in the EoS parameters of the two solid phases which define each triple

688   point, while the size of the gaps between them are proportional to the magnitude of the volume

689   decrease across the two transitions. Note: the fit to the B20 liquidus is constrained to pass through

690   both triple points.

691

692   **Figure 6**

693   *In situ* LH-DAC experiment 31A at 29 GPa. (a) Temperature vs. laser power plot. Open circles with

694   plus sign: *Pmmn* + B20-NiSi; Solid black circles: B20-NiSi + unknown trace phase (see text). The

695   dashed line represents the temperature above which the *Pmmn* phase was no longer observed and

696   the grey bar represents the melting temperature determined from the points within the melting

697   plateau, which are colour coded as a function of laser output. The open circles represent XRD

698   patterns in which LDS was observed. (b) XRD patterns colour coded to match (a). The black

699   dashed line represents the background fit to the pattern collected immediately before LDS was

700   observed. Tick marks from top to bottom represent B1-NaCl, B2-NaCl, B20-NiSi and the

701   unidentified trace phase (see text).

702

703   **Figure 7**

704   XRD patterns (black crosses) from experiment 31A (29 GPa) fitted with the LeBail method using

705   GSAS (red lines). (a) before heating, (b) at 1650 K, (c) at 1710 K and (d) after heating. Tick marks

706   from top to bottom represent B1-NaCl, B2-NaCl, B2-NiSi, B20-NiSi, B31-NiSi and the *Pmmn*

707   phase. The arrows denote the peaks associated with the unidentified trace phase (see text).

708

709   **Figure 8**

710   Melting data for selected Fe-Ni-Si alloys. The solid line is a fit to the *in situ* LH-DAC melting data

711   for $Fe_{91}Si_9$ of Fischer et al. (2013) that includes melting brackets, in which the appearance of LDS

712   was the melting criterion (open triangles), and melting points in which plateaux in temperature vs.

713   laser power curves were used (solid circles). The dashed line is a fit to the *in situ* LH-DAC melting

714   brackets (solid triangles) for $Fe_{85}Ni_5Si_{10}$ of Morard et al. (2011). Open circles are the melting data

715   for $Fe_{85}Ni_5Si_{10}$ from this study in which plateaux in temperature vs. laser power curves were used to

716   define melting.

717

718   **Figure 9**

719   Melting plateaus from off-line LH-DAC experiment 41 ($Fe_{85}Ni_5Si_{10}$) with symbols as in Fig. 3. (a)

720   Run 41A at 47 GPa. Only the right side is plotted due to a fault on the left side. (b) Run 41B at 49

721   GPa. The small (~80 K) difference in the plateaux temperature between the left and right sides is

722   most likely due to small misalignments between the heated spot and the spectrometer. (c)

723   Photomicrograph of the left side of the sample taken after laser heating. The dark spot resulting

724   from runs A and B are marked by the arrows. The white circle represents the location of a third

725   heating run, halted at 2000 K. Note the lack in the latter position of any change in the nature of the
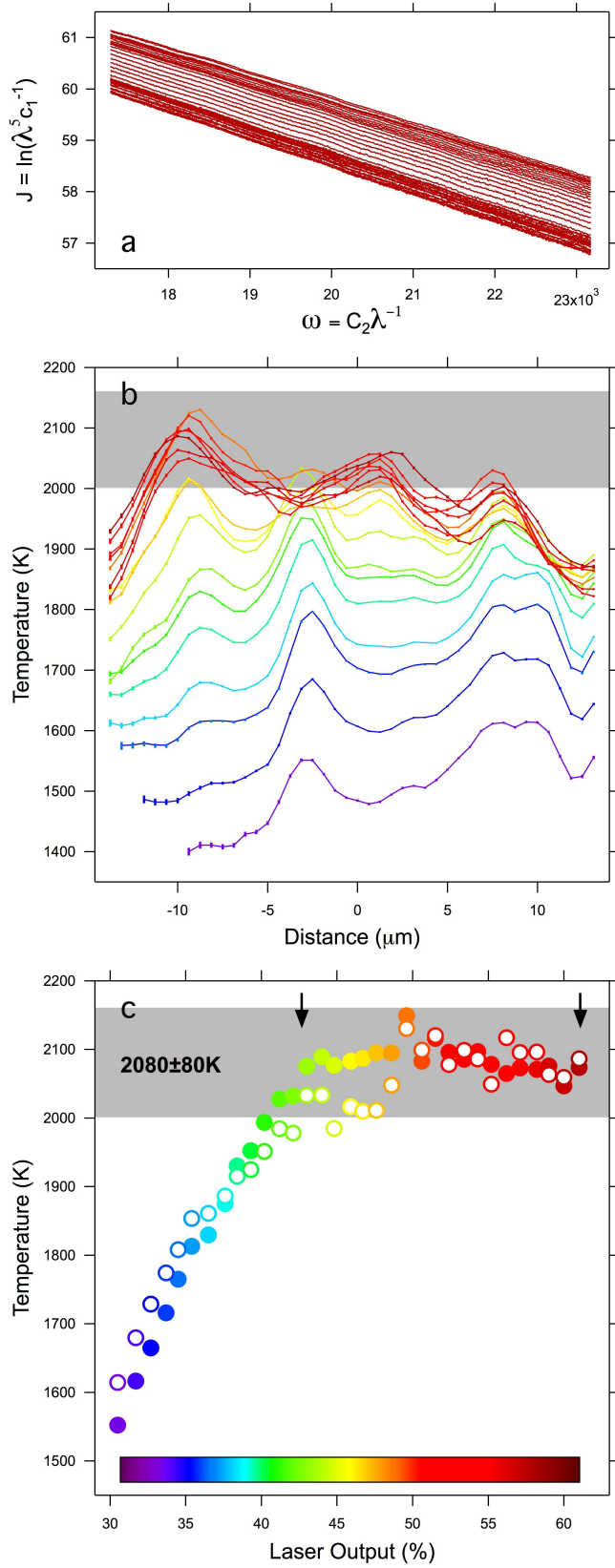
726   sample surface.

727
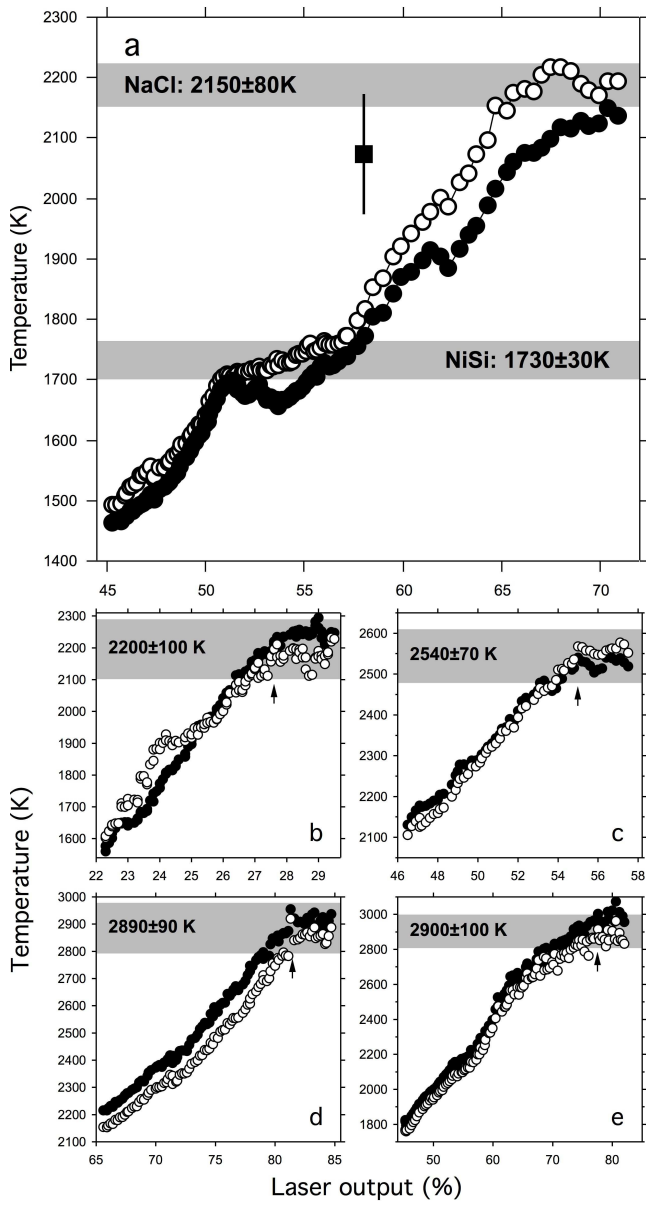
728   **Figure 1:**
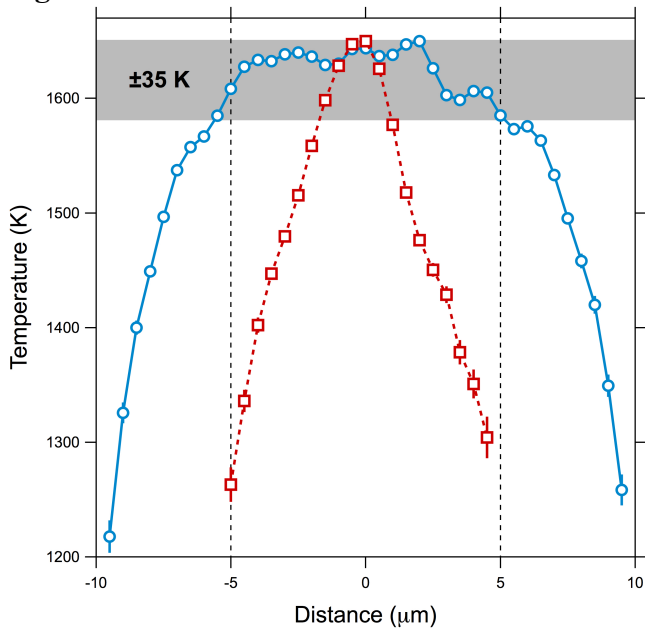
729

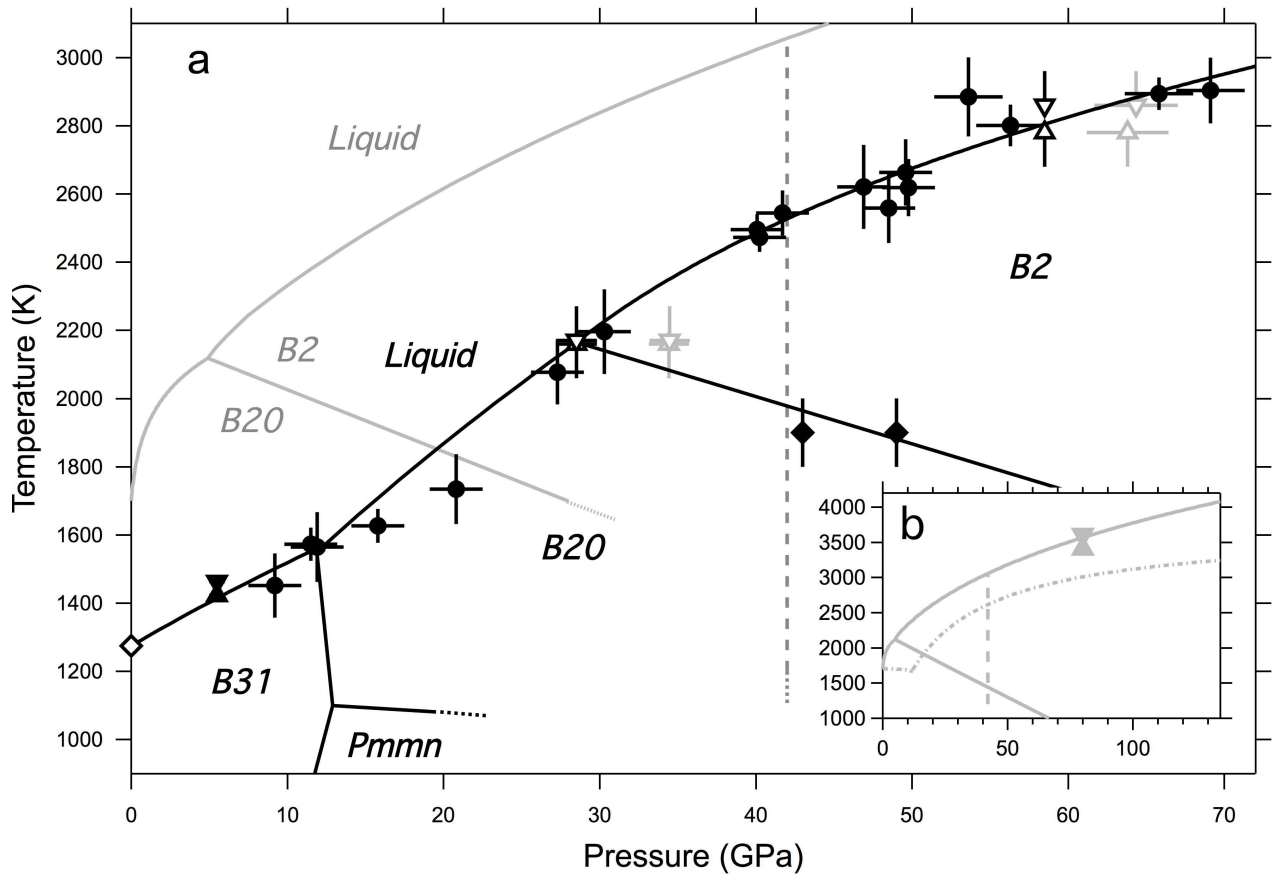730

731   **Figure 2:**

732
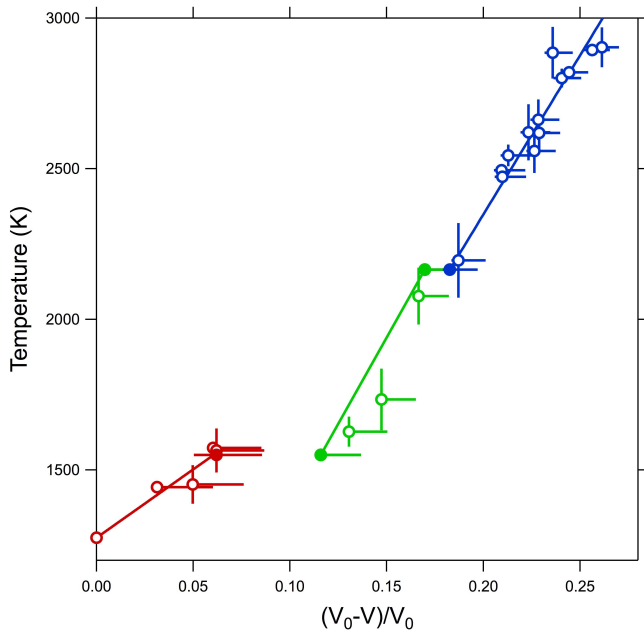
733   **Figure 3**

734

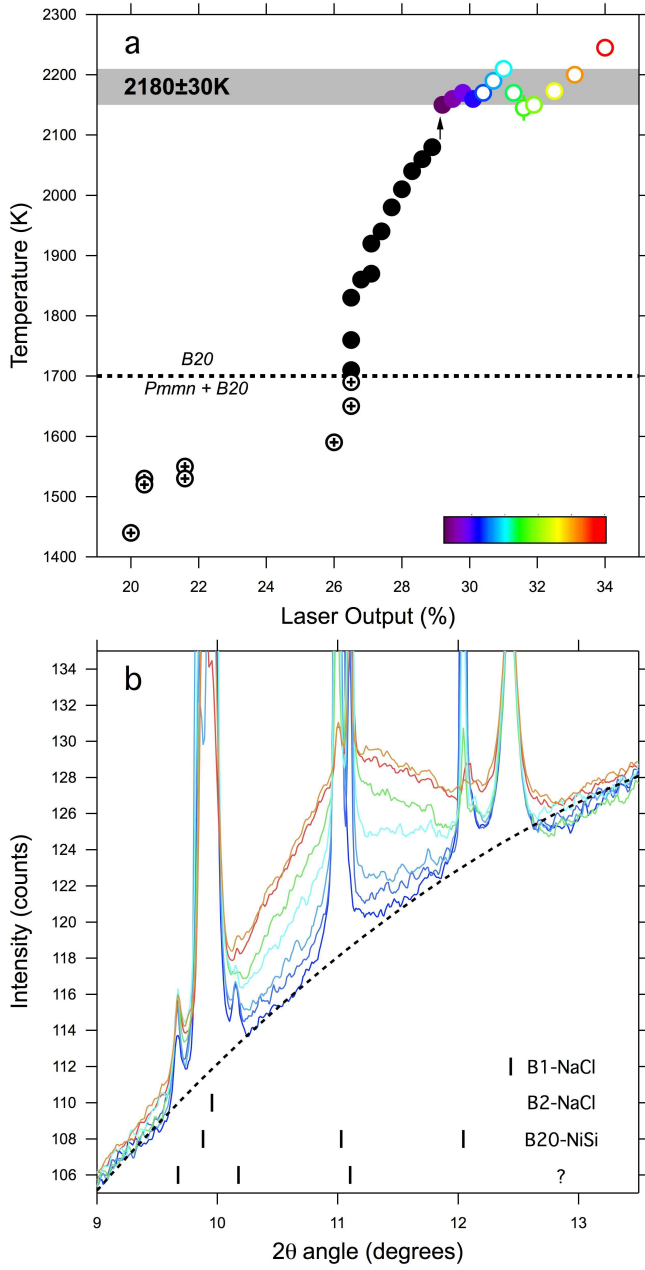735

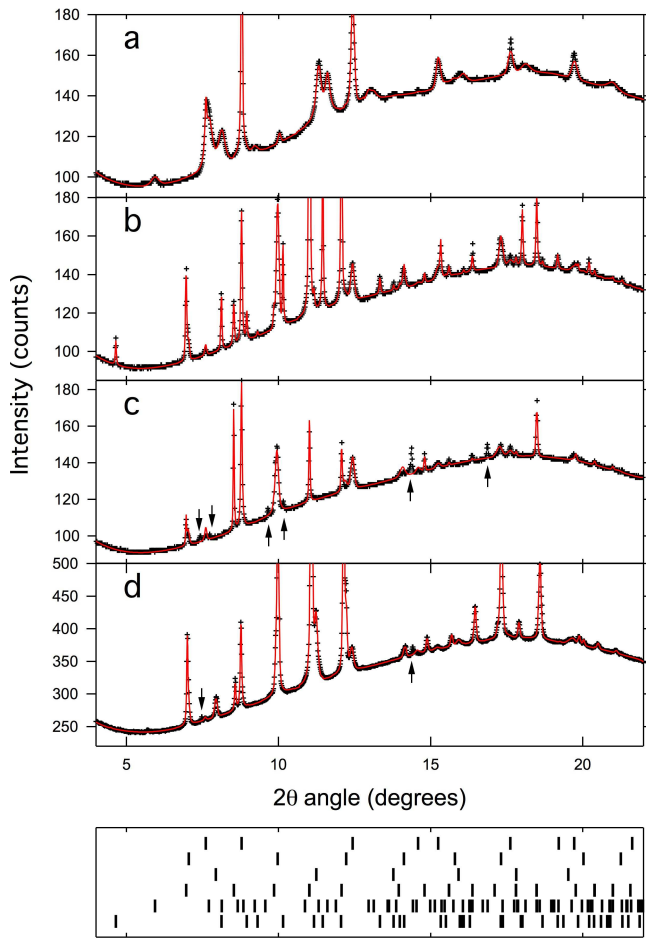736   **Figure 4**

737

738

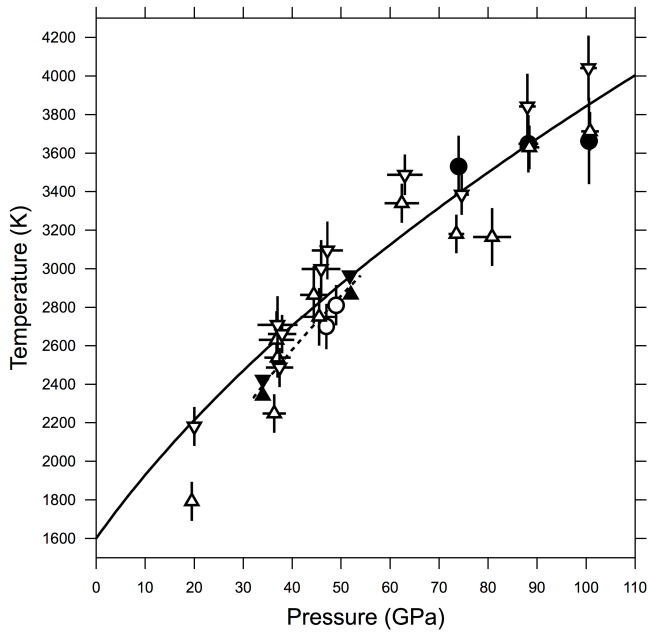739 **Figure 5**

740

741   **Figure 6**
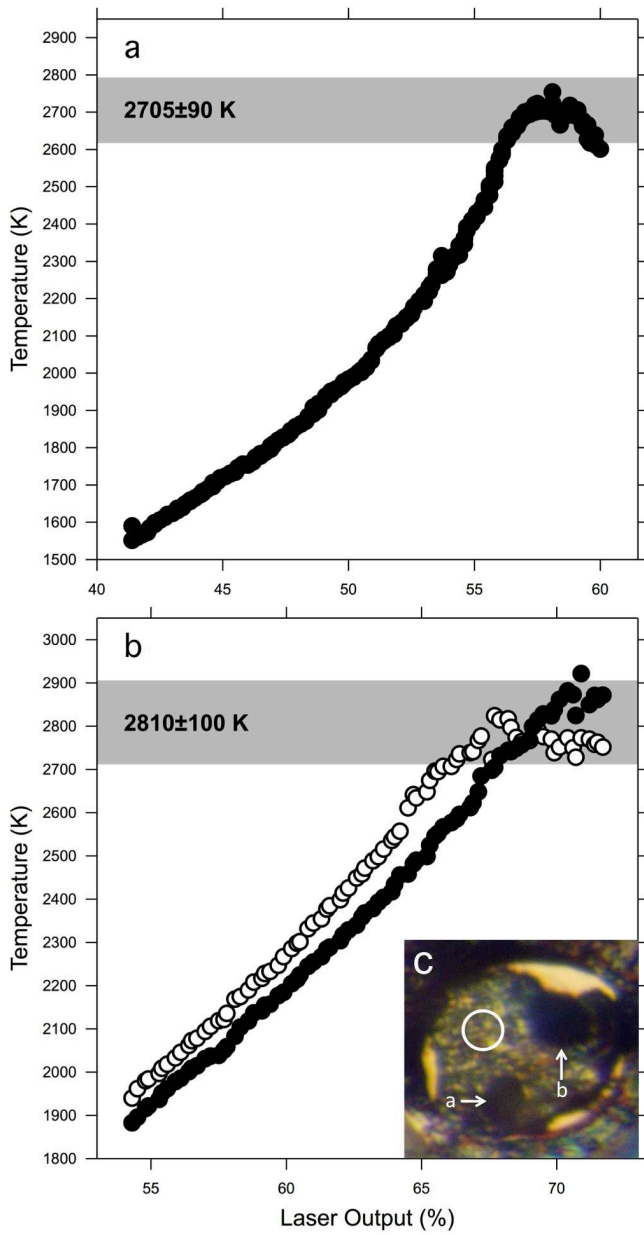

742

743

744   **Figure 7**

745

746   **Figure 8**

747

748

749   **Figure 9**

750

751

752 **Table 1:** NiSi melting data

Code	Pressure (GPa)	Temperature (K)
Off-line LH-DAC experiments (NiSi)		
24A	9.2±1.7	1452±94
26B	11.5±1.7	1573±49
26C	11.9±1.7	1565±103
25A	15.8±1.7	1627±50
25B	20.8±1.7	1734±102
25D	27.3±1.7	2077±94
40B	30.3±1.7	2196±124
57A	40.1±1.7	2495±45
57B	40.2±1.7	2473±42
28C	41.7±1.7	2544±66
25E	46.9±1.7	2621±123
28D	48.5±1.7	2559±103
57D	49.6±1.7	2663±97
57E	49.8±1.7	2619±84
28E	53.6±2.2	2885±116
57F	56.3±2.2	2801±61
57I	65.8±2.2	2894±48
29A	69.1±2.2	2903±96
in situ LH-DAC experiments (NiSi)		
31A	28.5±1.3	2165±61
31B	58.5±0.3	2780±92
in situ MAP experiments (NiSi)		
NiSi-04	5.5±1.7	1443±50
Off-line DAC experiments ($Fe_{85}Ni_5Si_{10}$)		
41B	47±1.7	2705±118
41C	49±1.7	2810±136

753

754

755　　**Table 2:** Fitting parameters

Phase	Simon-Glatzel			Kraut-Kennedy	
	T_0 (K)	A (GPa)	C	T_0 (K)	C
MnP (B31)	1275[a,b]	10±5	4±1	1275[a,b]	3.5±0.2
CsCl (B2)	2165[a,c]	12.8±6.1	4.7±1.4	2165[a,c]	4.9±0.2

[a]Parameters kept constant during fitting
[b](Massalski et al. 1990)
[c]Value of T_0 taken from the B20 + B2 + L triple point (TP2) defined by *in situ* experiment 31A (§3).

756